Mutation rates and adaptive variation among the clinically dominant clusters of Mycobacterium abscessus

Nicoletta Commins
Harvard Medical School
Mark Sullivan
Harvard TH Chan School of Public Health
Kerry McGowen
Harvard TH Chan School of Public Health
Evan Koch
Harvard Medical School
Eric Rubin
Harvard TH Chan School of Public Health https://orcid.org/0000-0001-5120-962X
Maha Farhat (maha_farhat@hms.harvard.edu)
Harvard Medical School https://orcid.org/0000-0002-3871-5760

Article

Keywords:

Posted Date: May 18th, 2022

DOI: https://doi.org/10.21203/rs.3.rs-1620528/v1

Mutation rates and adaptive variation among the clinically dominant clusters of *Mycobacterium abscessus*

Nicoletta Commins[1], Mark R. Sullivan[2], Kerry McGowen[2], Evan Koch[1], Eric J. Rubin[2,3], Maha Farhat[1,4] *

[1] Department of Biomedical Informatics, Harvard Medical School, Boston, MA, 02115, USA.

[2] Department of Immunology and Infectious Diseases, Harvard T. H. Chan School of Public Health, Boston, MA, 02115, USA.

[3] Department of Microbiology, Harvard Medical School, Boston, MA, 02115, USA.

[4] Division of Pulmonary and Critical Care Medicine, Massachusetts General Hospital, Boston, MA, 02114, USA.

* Correspondence: maha_farhat@hms.harvard.edu

Abstract

Mycobacterium abscessus (*Mab*) is a multi-drug resistant pathogen increasingly responsible for severe pulmonary infections. Analysis of whole genome sequences (WGS) of *Mab* demonstrates dense genetic clustering of clinical isolates collected from disparate geographic locations. This has been interpreted as supporting patient-to-patient transmission, but epidemiological studies have contradicted this interpretation. Here we present evidence for a slowing of the *Mab* molecular clock rate coincident with the emergence of phylogenetic clusters. We find that clustered isolates are enriched in mutations affecting DNA repair machinery and have lower spontaneous mutation rates *in vitro*. We propose that *Mab* adaptation to the host environment through variation in DNA repair genes affects the organism's mutation rate and that this manifests

as phylogenetic clustering. These results inform our understanding of niche switching for facultative pathogens, and challenge the model of transmission as the major mode of dissemination of clinically dominant *Mab* clusters.

Introduction

Mycobacterium abscessus (*Mab*) is an emerging, multi-drug resistant pathogen that is increasingly responsible for opportunistic pulmonary disease, most commonly in patients with underlying structural lung conditions such as cystic fibrosis (CF)[1]. *Mab* is divided into three subspecies: *M. a. abscessus*, *M. a. massiliense*, and *M. a. bolletii,* the former two being the most clinically relevant subspecies[2]. Infections with *Mab* are associated with accelerated decline in lung function and can result in severe disseminated disease and/or loss of eligibility for lung transplantation. *Mab* infections are difficult to treat, requiring a prolonged antibiotic regimen with high rates of treatment failure[3].

Until recently, *Mab* infections were thought to be acquired independently by each patient from environmental reservoirs in soil or water. Large scale analyses of whole genome sequencing (WGS) of Mab clinical isolates have revealed that a large proportion of clinical isolates fall into several phylogenetically characterized clusters, often termed dominant circulating clones[4]. Isolates within these clusters have high core genome similarity that is not explained by point source outbreaks as they were sampled from diverse geographic origins. These observations have been interpreted as supporting widespread recent transmission, either through direct contact or indirectly through fomites, but a number of epidemiological studies have refuted person-to-person transmission as a major mode of *Mab* dissemination[5–11]. Reconciling these conflicting lines of evidence is important as they dictate public health practice and allocation of resources to protect vulnerable populations from infection. However, it is still unclear what role transmission plays in the emergence of *Mab* clusters.

While widespread transmission is one proposed explanation for the phylogenetic structure observed in *Mab*, it is important to consider other factors in the species' evolutionary history that may contribute. For example, ecological niche switching from environmental sources to a human host may introduce bottlenecks resulting in low diversity and effective population size. Another explanation is a change in mutation rates, either through changes in bacterial generation time or through adaptive genetic variation. A third consideration is sampling bias, where particular *Mab* lineages that cause more frequent, severe and/or persistent disease are more likely to be isolated and sequenced. Consistent with the latter hypothesis, previous work has shown that isolates within clusters are more likely to contain point mutations associated with antibiotic resistance and are associated with greater bacterial burden and lung inflammation in mice[4].

Interpreting tree structures in the context of population history is aided by phylogenetic dating, which translates genetic distances into time scale. Previous studies[4,9,12,13] have estimated molecular clock rates in *Mab* but these have been limited to subpopulations within clusters. Here we report on molecular clock rate estimation for the deep branches of the *M. a. abscessus* phylogeny and for within-host isolates belonging to clusters. We provide evidence for an evolutionary slow-down coincident with the expansion of clinically dominant clusters and propose that the emergence of dense phylogenetic clustering in *Mab* may result from genetically encoded changes to the mutation rate. These results indicate that transmission is not the only plausible explanation for the dense clustering observed in the *Mab* phylogeny, and that more research is needed to clarify the transmission dynamics of this emerging pathogen.

Results

Phylogenetic analysis confirms the presence of large, dominant clusters (DCs) spanning multiple geographies. We identified 1,629 *M. abscessus* isolates with publicly available whole genome sequencing (WGS) data and associated dates of collection (Extended Data Table 1). We

excluded isolates with likely contamination or low-quality assemblies (Methods). Among the 1,461 isolates passing quality filters, the majority (80.1%) were derived from *in vitro* culture of pulmonary samples. Of the 1,181 pulmonary isolates, 98.3% (1,161/1,181) were collected from patients with cystic fibrosis (CF), while the rest were collected from patients with no documented diagnosis. The dataset represented 483 patients with unique patient identifiers, with 59.6% (288/483) of patients contributing a single isolate, and the remaining contributing between 2 to 24 isolates sampled over time. Isolates originated from nine countries and were collected between 1998-2017, with the exception of the reference strain ATCC 19977 which was collected in 1957 (Figure 1B).

The majority (91.7%) of samples had ≥98% average nucleotide identity (ANI) with one of three reference genomes (Supplementary Table 1) representing each of the three Mab subspecies, consistent with the commonly used ANI threshold for bacterial subspecies. Isolates with <98% ANI with any subspecies were excluded from downstream analysis. The resulting dataset overrepresented clinically relevant subspecies of *M. abscessus*, with 93.9% belonging to either *M. a. abscessus* or *M. a. massiliense*. To better resolve true evolutionary relationships among samples, we defined and restricted analysis to the core genome for each subspecies, then further excluded predicted recombination events (Methods). We performed maximum likelihood (ML) phylogenetic analysis for each of the three *Mab* subspecies, using only the first isolate from each patient to focus on between-host diversity. The resulting subspecies trees confirmed the presence of multiple, globally distributed clades with dense phylogenetic clustering (Methods). We excluded clustering due to potential point source outbreaks by limiting to clusters containing isolates from more than one country and a minimum of three isolates for downstream analysis. In total, we confirmed 16 clusters (Extended Data Figure 1A) including four clusters with > 50 isolates, which we refer to here as dominant clusters (DCs). Isolates within clusters comprised 76.4% of isolates included in the phylogenetic analysis. The median pairwise distance in *M. a.*

abscessus DC 1 was 68 SNPs. For comparison, the mean pairwise distance across the subspecies trees were 5537, 4100, and 8034 SNPs for *M. a. abscessus*, *M. a. massiliense*, and *M. a. bolletii*, respectively. All four DCs contained isolates originating from three continents (North America, Europe, and Australia). Clustered isolates also spanned the full range of isolation times, including ATCC 19977, which was placed within *M. a. abscessus* DC 1 despite having been collected at least 40 years before any other isolates in the tree (Figure 1A-B).

Coalescent analysis reveals a faster long-term evolutionary rate than observed in DCs. To aid in transmission inference and to reconstruct the evolutionary history of *Mab*, we performed a coalescent analysis using our SNP alignment. Previous work has reported molecular clock rates within *Mab* clusters, but to our knowledge no study has successfully dated any of the full *Mab* subspecies phylogenies. To evaluate the presence of temporal signal, we performed root-to-tip regression for each subspecies tree but in each case did not observe a positive correlation between sampling date and root-to-tip distance. We reasoned that the high degree of population structure in the *Mab* phylogeny may obscure the genetic-temporal signal. To test this hypothesis, we pruned each subspecies tree until it contained the minimal number of samples required to capture 95% of the genetic diversity in the original tree (Methods). Following pruning of the *M. a. abscessus* subspecies tree, root-to-tip regression demonstrated the presence of temporal signal (Figure 1C, D). Evidence of temporal signal in *M. a. abscessus* was further strengthened using a permutation test and a Bayesian evaluation of temporal signal (Extended Data Figure 1C, Extended Data Table 3).

We used a Bayesian implementation of coalescent analysis, BEAST[14], to estimate the molecular clock rate of the pruned *M. a. abscessus* subspecies tree assuming a relaxed clock model, which allows each branch of the tree to have its own clock rate. To explore the effect of the tree prior on molecular clock estimation, we ran analyses using two different tree priors, assuming either a constant coalescent model, which assumes constant population size over time,

or a Bayesian skyline coalescent model, which allows the population size to change over time. While the Bayesian skyline coalescent had a slightly better marginal likelihood, we found no significant difference between the clock rates estimated by the two models (Table 1, Figure 2C). Our estimates for the clock rate in the long, internal branches of the tree were approximately 10-fold faster than nearly all previously reported estimates of the clock rate within *Mab* clusters (Figure 2C). We next attempted to date the full (unpruned) *M. a. abscessus* phylogeny using the faster rate inferred from our coalescent analysis of the pruned tree. These chains suffered from poor convergence and sampled trees with a distorted topology, elongating the short branches and eliminating the densely clustered structure observed in the ML phylogeny (data not shown). We therefore hypothesized that the lack of temporal signal in the full *M. a. abscessus* dataset may result from a difference between the long-term clock rate and the more recent evolutionary rate within phylogenetic clusters.

Analysis of longitudinally sampled within-host isolates supports a slower clock rate in DCs. To further investigate the differences in clock rate between long-term historical time scales and short-term contemporary time, we used pairs of isolates sampled from the same patient over time to estimate the mutation rate. We focused on estimating a within-host clock rate for *M. a. abscessus* to compare directly with the estimate from our coalescent analysis and because we had the most longitudinal samples for this subspecies. Because polyclonal *Mab* infection is common in CF patients, we first excluded any isolate pairs with a SNP distance > 20. This threshold was selected by comparing the distribution of all possible within-host isolate pairs to the distribution of pairwise SNP distances within *Mab* clusters (Figure 2A, Extended Data Figure 2). Regressing the SNP distance between isolate pairs on the time between sample pairs yielded a mutation rate of 2.21 SNPs/year [1.06 – 3.37 95% CI], or 5.17×10^{-7} SNPs/site/year [2.48×10^{-7} – 7.92×10^{-7} 95% CI]. This value is more comparable to previously reported molecular clock rate estimates within *Mab* clusters[4,9,12,13] than to those estimated in the long branches of the phylogeny (Figure 2C).

Simulated ancestries support mutation rate slow-down over population size effects as the major driver of phylogenetic clustering. To test whether sampling from clades with low genetic diversity is sufficient to explain the degree of clustering observed in the ML phylogeny, or whether changes in the molecular clock rate are a better explanation for the observed phylognetic data, we performed coalescent simulations of ancestries with one clustered subpopulation (A) and one unclustered subpopulation (B). Under a range of effective population sizes (N_e) and mutation rates (μ), we simulated ancestries through time with 1000 replicates per simulation. For each replicate we assessed the degree of phylogenetic clustering by measuring d_A/d_B where d_i is the mean pairwise SNP distance within subpopulation i. The total N_e (N_e^T), number of samples, and sampling dates for subpopulations A and B were drawn from the true values for *M. a. abscessus* DC 1 and from all "unclustered" isolates in our dataset, respectively (Figure 3A). We first tested whether a smaller population size for the clustered subpopulation A (N_e^A) could explain the degree of phylogenetic clustering observed. We estimated a range of realistic values for N_e^A using BEAST by assuming a range of possible clock rates (Extended Data Table 4). These rates spanned a published clock rate estimate for *M. a. abscessus* DC1 to a clock rate that is 50-fold higher, far exceeding the upper 95% highest posterior density (HPD) interval for the published value[13] Under the the simulated conditions of equal mutation rates between subpopulation A and B, we only observed phylogenetic clustering to the extent observed in the clinical isolate phylogeny in the scenario where $N_e^T >> N_e^A$ (Figure 3B, Extended Data Figure 3). We next tested whether a change in the mutation rate at the root of supopulation A could better explain the observed phylogenetic structure in *Mab*. The simulated ancestries where N_e^A and N_e^B are fixed and the mutation rate slowdown is between 10- and 20-fold recapitulated the observed phylognetic structure (Figure 3C). This result was robust to changes in N_e^A and N_e^T across the 95% HPD for each parameter (Extended Data Figure 4). These results indicate that for person-to-person transmission to drive phylogenetic clustering in *Mab*, the total N_e must be very large compared to the N_e of the clustered

179 subpopulation, an unlikely scenario given the observed genetic data and sampling times. By
180 contrast, a mutation rate change of 10- to 20- fold explains the degree of clustering observed in
181 *Mab* under more realistic population sizes given these data.
182
183 UvrD/Rep family helicases are enriched in DCs in *M. a. abscessus*. To identify genetic variants
184 under positive selection in *Mab* clusters, we searched for evidence of phylogenetic convergence
185 in the core genome of *M. a. abscessus* with regions of recombination excluded. Briefly, we
186 performed ancestral sequence reconstruction for the internal nodes of the subspecies tree and
187 counted the number of independent arisals of each SNP (Methods). Of the 65,202 SNPs identified
188 in *M. a. abscessus*, 34,813 (53.4%) of mutations occurred only once and were excluded. For the
189 remaining SNPs, we ranked each by its enrichment in DCs relative to other regions of the *M. a.*
190 *abscessus* tree (Figure 4A). The most significantly enriched variants in the *M. a. abscessus* DCs
191 included homologs of several known or putative virulence factors as well as a number of cluster-
192 enriched mutations in UvrD-like helicases *MAB_1054*, *MAB_3515c*, and *MAB_3516c* (Table 2,
193 Figure 4A). While the function of these genes is not well characterized in *M. abscessus*, all three
194 share homology with the UvrD/Rep family of helicases. This family of genes is involved in DNA
195 repair and has been associated with growth and persistence *in vivo*[15,16].
196
197 Isolates in *Mab* DCs are associated with a lower spontaneous mutation rate. To test the
198 association between phylogenetic clustering and spontaneous mutation rate, we selected *M. a.*
199 *abscessus* and *M. a. massiliense* strains that were grouped within DCs or that were not present
200 in those clusters. Each of the strains present in the DCs has the derived (minor) allele at four sites
201 in the UvrD/Rep family genes *MAB_1054*, *MAB_3515c*, and *MAB_3516c*, and the strains outside
202 of DCs possess the ancestral (major) allele at those sites (Table 2, Figure 4A). The strains used
203 and their genotypes are described in Supplementary Data Tables 2 and 3. The spontaneous
204 mutation rate was estimated in all strains using a fluctuation assay[17] adapted for use in *M.*

abscessus. The fluctuation assay counts cells gaining resistance to the antibiotic amikacin during growth in culture without antibiotic. By normalizing the number of mutational events to the population size of the culture, the fluctuation assay estimates the spontaneous mutation rate per generation per the number of bases that can be mutated to confer resistance to amikacin. The strains chosen display similar growth rates (Extended Data Figure 5) and very low baseline resistance to amikacin (Extended Data Table 5) which allows them to be compared using a fluctuation assay. Among *M. a. abscessus* strains, those present in DCs with the derived (minor) allele at the four UvrD/Rep loci had lower spontaneous mutation rates than those with the ancestral (major) allele (Figure 4C). A similar trend was observed in *M. a. massiliense* strains (Figure 4D). Further, the average mutation rate was significantly lower in isolates present in DCs across both subspecies (Figure 4E), consistent with the hypothesis that the emergence of dense clustering may be driven in part by changes in mutation rate.

Discussion

In this study we have pooled a large global sample of *Mab* genome sequences and examined evolutionary rates and positive selection with the goal of understanding the emergence of *Mab* clusters. We present evidence supporting a slower evolutionary rate within DCs compared to the long internal branches of the phylogeny and further data associating adaptive genetic variation in DNA repair genes with the slower evolutionary rate. We posit that changes to the mutation rate underlie the dense clustering in *Mab*, and that while other effects such as population or transmission bottlenecks and sampling bias may contribute to the low genetic diversity within clusters, they are not sufficient to explain the observed phylogenetic structure.

Previous studies have restricted molecular clock rate estimation to *Mab* clusters, most likely because of the lack of temporal signal at the subspecies-level. By pruning the *Mab* tree while preserving the majority of the subspecies diversity, we were able to measure a molecular clock rate for *Mab* spanning the time scale from the common ancestor of the subspecies to the

present. Estimates of evolutionary rates are recognized to depend on the time scale of measurement. In such examples, the clock rate usually decreases with increasing time depth[18]. We observe the opposite effect where the clock rate increases with time depth. The pruned *Mab* tree most likely reflects an evolutionary process taking place predominantly in environmental reservoirs, in contrast to phylogenetic clusters where terminal branches reflect evolution within the human lung environment. We also note that our measurement of within-host mutation rate in *Mab* was independent of phylogenetic inference and the full temporal signal in our sample. Nevertheless, the measured rate within-host was comparable to the clock rate measured previously using coalescent analysis within clusters (Figure 2C).

The molecular clock rate is influenced by both the spontaneous mutation rate and the generation time of an organism. Changes in generation time could result from physiological constraints of the human lung environment, if for example, differences in nutrient availability change the growth rate in the lung compared to those living in environmental reservoirs. Generation times and spontaneous mutation rates can also be modified by genetic changes, for example to DNA replication or repair machinery. The observation that some lineages have adapted to the host environment [4] raises the possibility that genetic changes that underlie or associate with this adaptation affect mutation rate, either directly by affecting DNA replication or repair machinery, or indirectly by affecting the growth rate. Ruis et al. reported differences in mutational signatures along internal branches of the subspecies phylogeny compared to internal branches of DCs, supporting a change in the mutational process within some clades of the tree[13].

We scanned the core genomes for variants enriched in the DCs in *M. a. abscessus*, the subspecies for which we have the most WGS data and for which there are the highest number of clusters. Notably, we observed several cluster-enriched mutations in UvrD-like helicases. UvrD is a superfamily 1 helicase that is involved in DNA repair and is widely conserved in gram-negative bacteria. UvrD1 in *M. tuberculosis* plays an important role both in nucleotide excision repair (NER) and in pathogenesis and persistence because its DNA repair activity confers tolerance to reactive

oxygen intermediates (ROI) and reactive nitrogen intermediates (RNI)[15]. Mutations that promote the activity of UvrD1 and its homologs are likely advantageous in the context of lung infection and may have the additional consequence of decreasing the spontaneous mutation rate. We additionally observed mutations in UvrD-like helicases occurring along the cluster-defining branch of the large *M. a. massiliense* cluster, further supporting the role of the NER pathway in *Mab* pathogenesis.

Our study has several limitations. Our dataset overrepresented clinical isolates from the UK where routine whole genome sequencing is part of *Mab* surveillance. Oversampling of some lineages and geographies may mean that we have not adequately captured the global population structure and that we may have focused on large phylogenetic clusters because of their geographic distribution and not because of their clinical significance. While our study argues against transmission as the main driver of *Mab* dissemination and the emergence of DCs, we do not examine the geographic distribution of Mab within clusters. It is possible that future work considering this data can highlight mechanisms of parallel evolution that explain why clustered *Mab* isolates are detected in distant geographic locations. While our results support a faster molecular clock rate in the long internal branches of the phylogeny compared to clustered lineages, we are unable to distinguish between rate differences due to the spontaneous mutation rate from generation time effects. Differences in growth conditions across environments is difficult to quantify as *Mab* is ubiquitous in both natural and built environments, but nutrient availability likely differs greatly between natural reservoirs such as soil and water compared to man-made reservoirs such as showerheads. A healthy lung supports relatively little bacterial growth, but inflammation increases nutrient availability by promoting mucus production and vascular leakage into the airway [19]. Because there is little publicly available sequencing data from environmental isolates, we were also unable to compare genotypes or mutation rates in environmental samples compared to clinical isolates. Our analysis of variants associated with phylogenetic clustering is

also limited in its ability to identify true causal genotypes or those that are enriched in clusters due to hitchhiking to other adaptive variants.

In summary, we present new evidence for changes in the molecular clock rate that contribute to the dense phylogenetic clustering observed in *Mab*. These results argue against person-to-person transmission as the primary driver of clustering in the *Mab* phylogeny. Continuing genomic surveillance is needed to understand how *Mab* may be adapting to human infection and to characterize the risk of transmission to at-risk patients. We argue further that the phylogeographic structure of *Mab* is influenced by its complex ecological history as an emerging facultative pathogen that should be considered carefully in future analysis of *Mab* genomic data. Future work should extend these analyses by examining differences in mutation rates and phenotypes between clinical isolates and environmental strains for evidence of host adaptation.

Acknowledgements

We thank members of the Farhat lab for feedback and discussion. We are grateful to Luca Freschi for advice on processing WGS data, calling variants, and phylogenetic inference; Maximillian Marin for input on calculating mappability pileup; and Roger Vargas for support in homoplasy counting. We also thank Wilder Wohns for discussions on implementing ancestry simulations with mutation rate changes through time. M.R.S. is a Merck Fellow of the Damon Runyon Cancer Research Foundation, DRG-2415-20. Computational resources and support were provided by the Orchestra High Performance Compute Cluster at Harvard Medical School, which is funded by the NIH (NCRR 1S10RR028832-01).

Author Contributions

Conceptualization, N.C. and M.F.; Methodology – Computational analysis, N.C., E.K., and M.F.; Methodology – Experimental studies, M.R.S., K.M.; Investigation – Computational analysis, N.C.;

Investigation – Experimental studies, M.R.S., K.M.; Data Curation, N.C.; Writing – Original Draft, N.C. and M.R.S.; Writing – Review & Editing, N.C., M.R.S., E.K., M.F.; Supervision, E.J.R., M.F.

Declaration of Interests

The authors declare no competing interests.

Tables

Table 1. Coalescent analysis results and model comparison

Model	**Marginal Log Likelihood (SD)**	**UCLD Rate (SNPs/site/year)**	**UCLD St. Dev.**
Coalescent constant population	-7144301.64 (21.42)	2.82×10^{-6} [1.33×10^{-6}, 4.83×10^{-6}]	0.182 [0.135, 0.234]
Bayesian skyline coalescent	-7144118.76 (19.93)	2.63×10^{-6} [1.16×10^{-6} , 4.0×10^{-6}]	0.181 [0.138, 0.232]

Table 2. Summary of top 10 nonsynonymous variants enriched in DCs of *M. a. abscessus*

Gene	Gene Symbol	Description	Comments	Enrichment p-value	Number of clustered taxa containing variant	Number of unclustered taxa containing variant
MAB_3334c	*gatB* [c]	Aspartyl/glutamyl-tRNA (Asn/Gln) amidotransferase subunit B [c,d]	Essential for growth and survival *in vivo* in *M. tuberculosis* [17]	1.03×10^{-65}	240	1
MAB_3244		Mercury resistance transport protein/cytochrome c biogenesis protein [c]		1.72×10^{64}	189	3
MAB_3480		Putative short chain dehydrogenase/ Reductase [c]		7.23×10^{-64}	232	13
MAB_4141[a]		PE/PPE family protein [c]		1.58×10^{-62}	189	2
MAB_3242	*fni* [c]	Isopentenyl-diphosphate delta-isomerase [c,d]		8.07×10^{-62}	189	3
MAB_3481	*fadE* [c]	Probable acyl-CoA dehydrogenase [c]	FadE mutations in *Mtb* result in decreased growth and virulence in macrophages and in mice[18]	2.10×10^{-61}	232	15
MAB_4057c	*mshA* [c]	D-inositol 3-phosphate glycosyltransferase [d]	Catalyzes biosynthesis of mycothiol, an important compound in resisting oxidative stress and detoxifying harmful agents such as antibiotics[19]	2.78×10^{-60}	189	2
MAB_3581c		Hypothetical protein		6.09×10^{-60}	169	3
MAB_1054[b]	*pcrA*[c] / *uvrD1*[d]	ATP-dependent DNA helicase [c,d]	Involved in nucelotide excision repair (NER), mismatch repair (MMR), homologous recombination (HR), and rolling circle replication[15]	2.72×10^{-58}	216	7
MAB_3515c	*rep* [c,d]	ATP-dependent DNA helicase [c,d]	Involved in NER, MMR, HR and rolling circle replication[15]	8.42×10^{-57}	189	7

Table 2 Legend:

[a] Multiple variants in *MAB_4141* have been collapsed and the lowest p-value is shown. See Supplementary Material for full list of homoplasic SNPs ranked by their enrichment in clusters.

[b] Gram-negative bacteria possess UvrD and a closely related homolog, Rep, while gram-positive bacteria possess a single homolog called PcrA.[20]

[c] Mycobrowser annotation

[d] prokka annotation

Figures

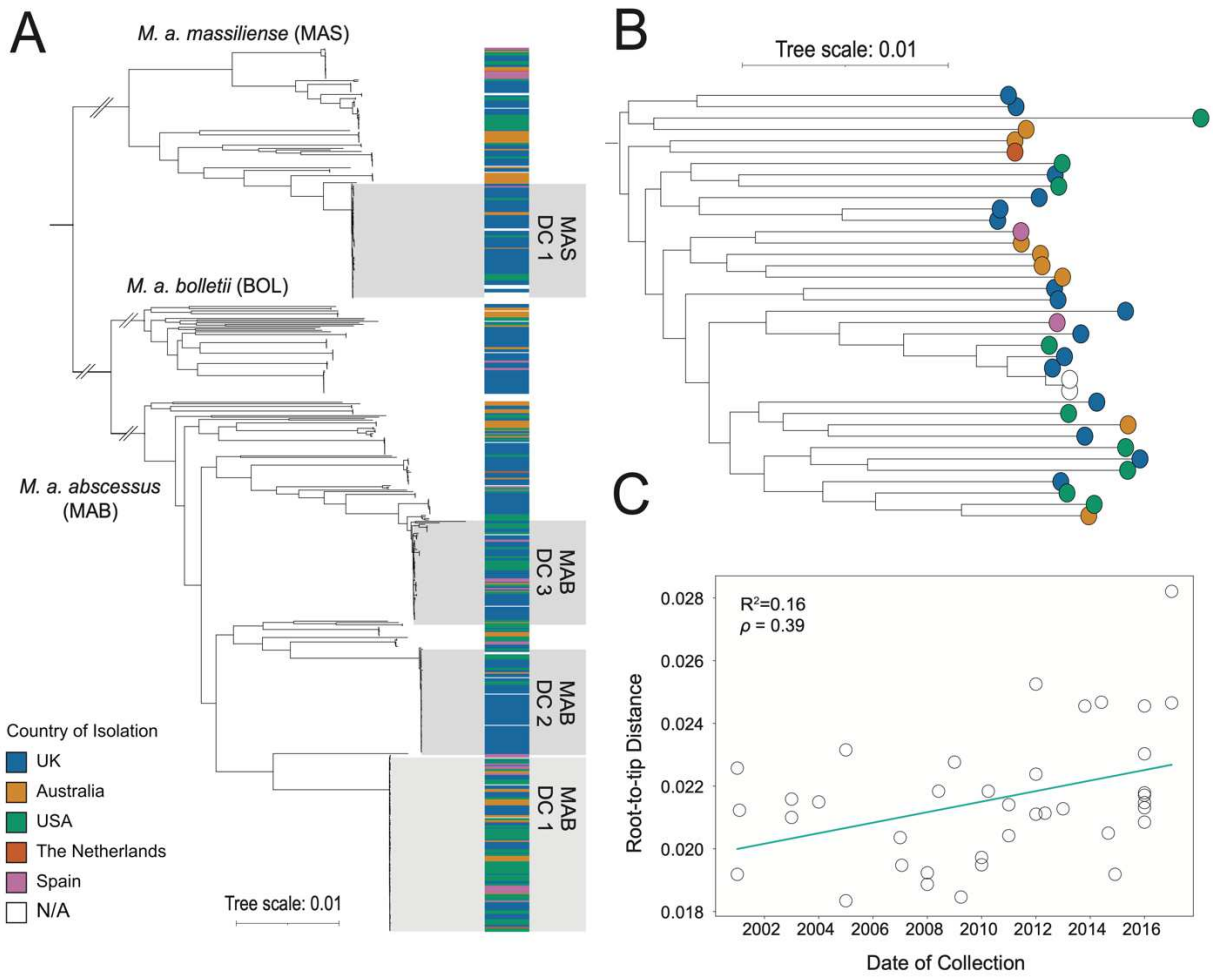

Figure 1. Dominant clusters of *M. abscessus* and the presence of temporal signal in internal branches. A) Species-wide phylogeny of *M. abscessus* representing one isolate per patient to avoid within-patient clustering of samples. Each subspecies tree was constructed independently using a subspecies specific reference genome. The four largest phylogenetic clusters are highlighted. B) Histogram showing the distribution of collection dates of all clustered isolates v. all unclustered isolates in *M. a. abscessus*. C) Pruned *M. a. abscessus* phylogeny representing 95% of the original subspecies tree diversity. C) Root-to-tip regression showing evidence of positive temporal signal in the pruned tree shown in (B).

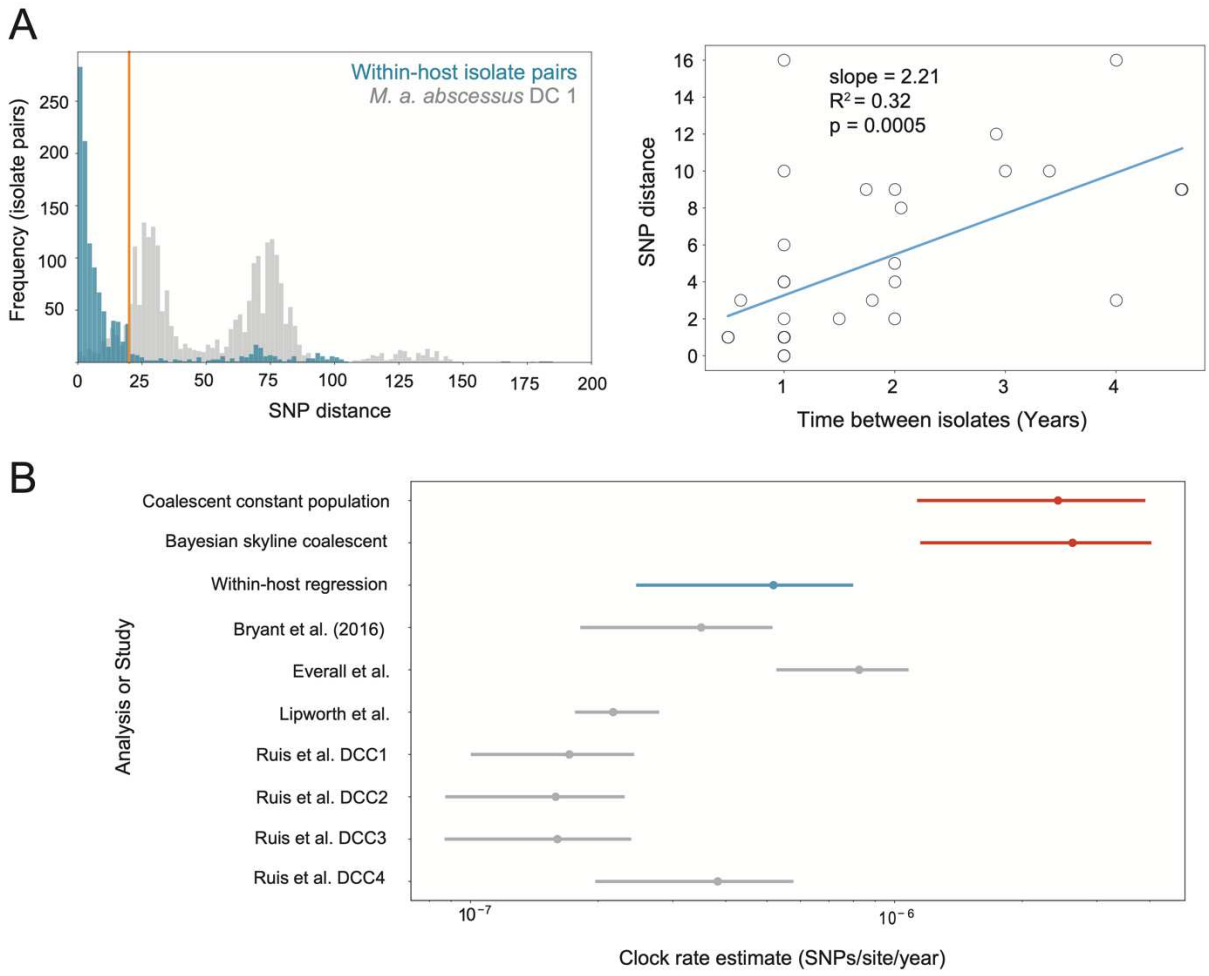

Figure 2. Longitudinally sampled within-host isolates and coalescent analysis support a slower clock rate within DCs. A) Clock rate estimation using isolate pairs sampled from the same patient over time. Left: distribution of SNP distances between all possible within- host isolate pairs compared to SNP distances between all possible isolate pairs within *M. a. abscessus* DC 1. The orange line represents the threshold of 20 SNPs used to exclude pairs representing independent infections. Right: regression of SNP distance on the time between isolates for each isolate pair. The slope of the regression line was 2.51 SNPs/year [1.24 – 3.78 95% CI], or roughly 5.93×10^{-7} SNPs/site/year [2.92×10^{-7} – 8.9×10^{-7} 95% CI]. B) UCLD clock rate estimates for the three models used in this study (two coalescent models shown in red and one regression model shown in blue) compared to mutation rate estimates from the within-host regression (blue) and published clock rates (grey).

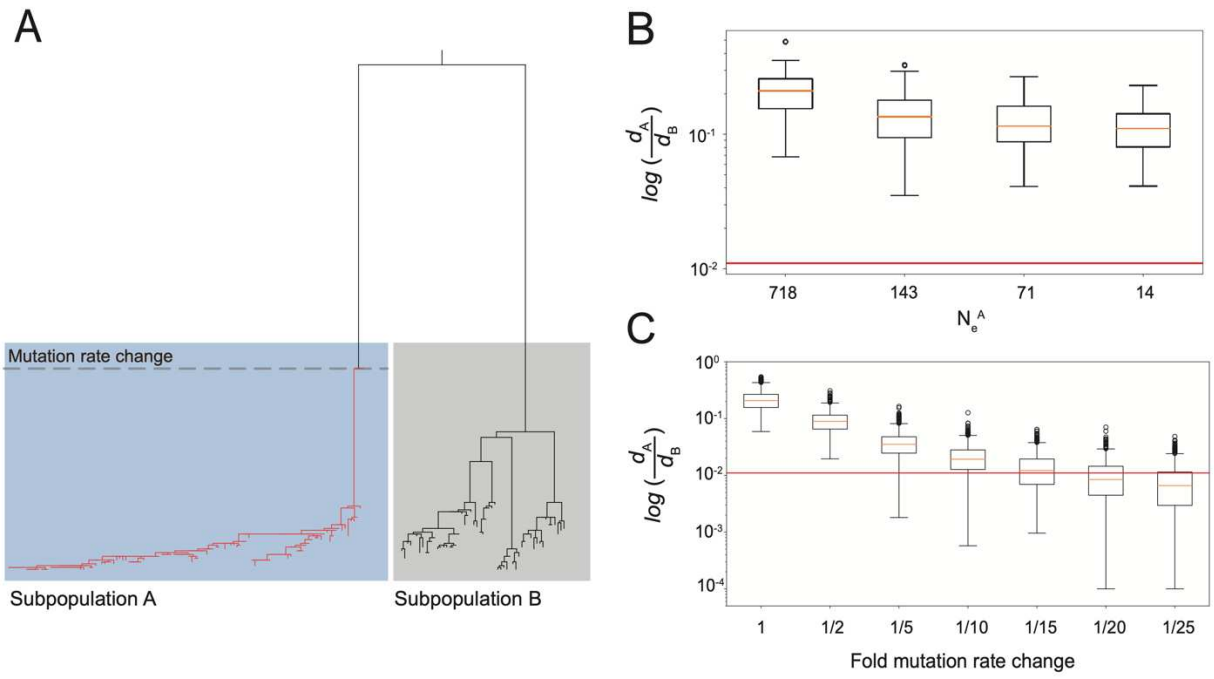

Figure 3. Simulated ancestries support a mutation rate slow-down coincident with DC emergence. A) Example neighbor joining (NJ) tree from the simulation shown in B. The number of samples and sampling dates for subpopulations A and B are drawn from real data from *M. a. abscessus* cluster 1 and from all unclustered samples, respectively. The dotted line crosses the common ancestor node for subpopulation A, and all branches descended from this node (shown here in red) are subject to the change in mutation rate. B) Boxplot showing the degree of phylogenetic clustering in subpopulation A relative to subpopulation B over a range of effective population sizes of subpopulation A (N_e^A). The simulation assumes that N_e^T=8000. C) Boxplot showing the degree of phylogenetic clustering in subpopulation A relative to subpopulation B over a range of mutation rate changes. The simulation assumes that N_e^T=8000 and N_e^A=718. In both A) and B) the degree of clustering is estimated with metric $\log(\frac{d_A}{d_B})$ where d_i is the mean pairwise SNP distance among all sample pairs in subpopulation i. The red line represents the clustering metric estimated using the observed ML phylogeny.

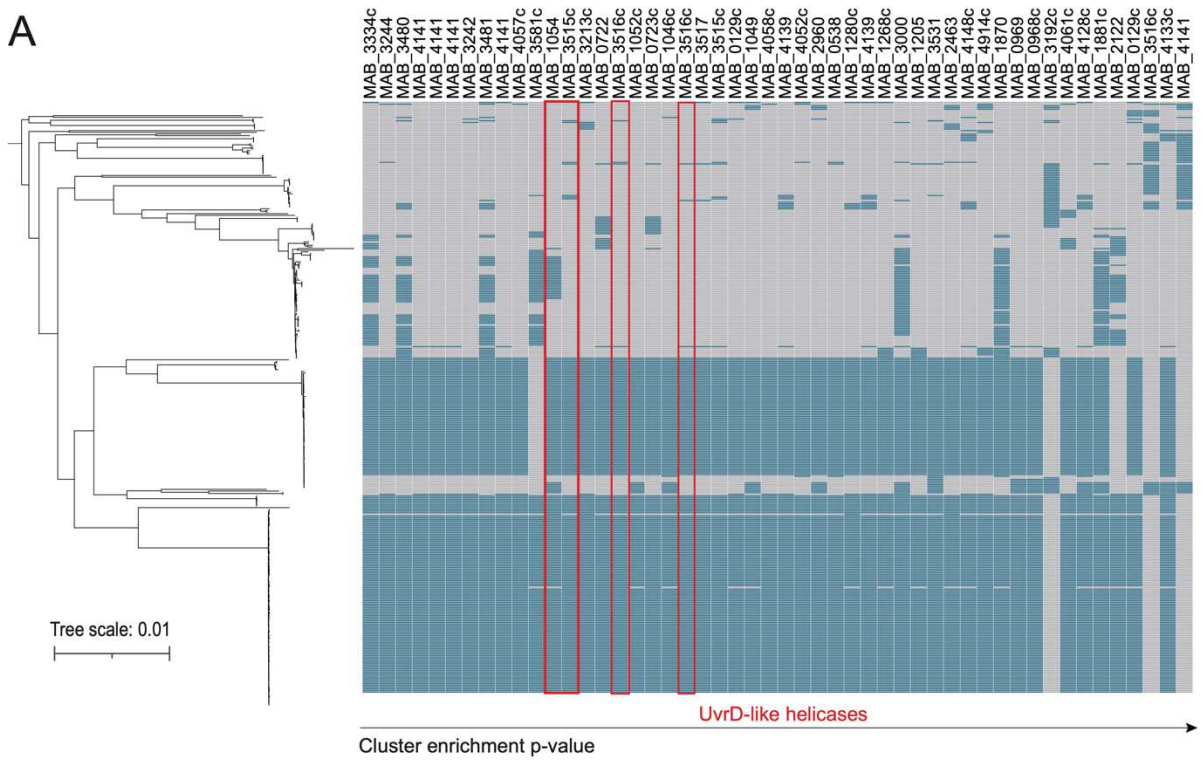
A
MAB_3334c
MAB_3244
MAB_3480
MAB_4141
MAB_4141
MAB_4141
MAB_3242
MAB_3481
MAB_4141
MAB_4057c
MAB_3581c
MAB_1054
MAB_3515c
MAB_3213c
MAB_0722
MAB_3516c
MAB_1052c
MAB_0723c
MAB_1046c
MAB_3516c
MAB_3517
MAB_3515c
MAB_0129c
MAB_1049
MAB_4058c
MAB_4139
MAB_4052c
MAB_2960
MAB_0538
MAB_1280c
MAB_4139
MAB_1268c
MAB_3000
MAB_1205
MAB_3531
MAB_2463
MAB_4148c
MAB_4914c
MAB_1870
MAB_0969
MAB_0968c
MAB_3192c
MAB_4061c
MAB_4128c
MAB_1881c
MAB_2122
MAB_0129c
MAB_3516c
MAB_4133c
MAB_4141
Tree scale: 0.01
UvrD-like helicases
Cluster enrichment p-value

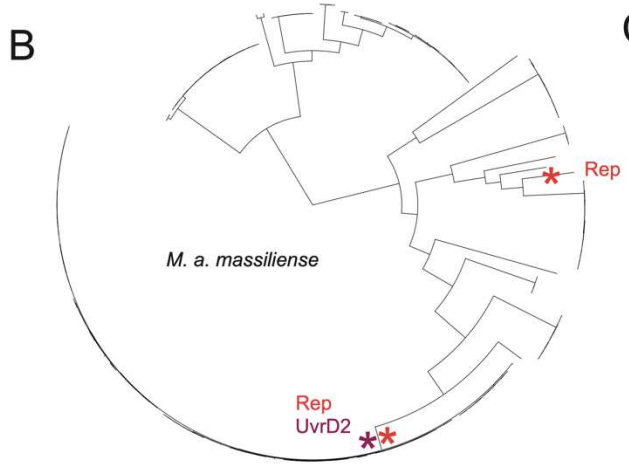
B
Rep
M. a. massiliense
Rep
UvrD2

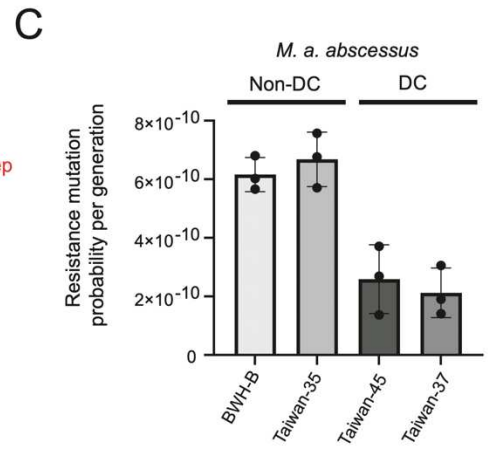
C
M. a. abscessus
Non-DC
DC
Resistance mutation probability per generation
8×10-10
6×10-10
4×10-10
2×10-10
0
BWH-B
Taiwan-35
Taiwan-45
Taiwan-37

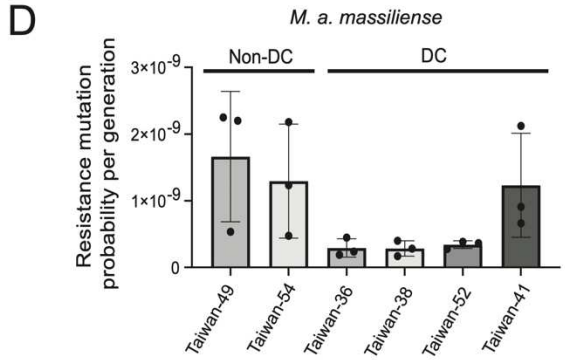
D
M. a. massiliense
Non-DC
DC
Resistance mutation probability per generation
3×10-9
2×10-9
1×10-9
0
Taiwan-49
Taiwan-54
Taiwan-36
Taiwan-38
Taiwan-52
Taiwan-41

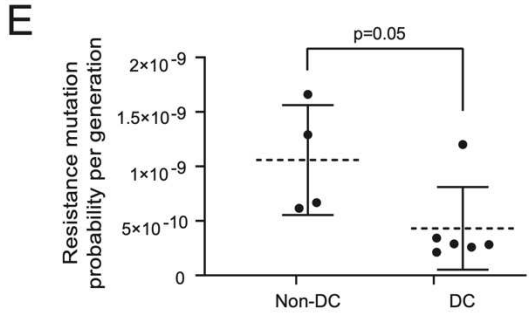
E
p=0.05
Resistance mutation probability per generation
2×10-9
1.5×10-9
1×10-9
5×10-10
0
Non-DC
DC

502

Figure 4. Dominant clusters are associated with a decrease in the spontaneous mutation rate *in vitro*. A) Subspecies phylogeny for *M. a. abscessus* (left) and corresponding heatmap representing the presence of the derived allele (blue) or ancestral allele (grey) for each nonsynonymous variant. Variants are ranked in ascending order by their p-value derived from Fisher's tests for enrichment in the three largest clusters. The top 50 hits are shown. The genes where each variant is located are denoted. B) Subspecies phylogeny for *M. a. massiliense*. The branches where mutations have occurred in homologs of Rep and UvrD2 are shown with asterisks. Probability of acquiring an amikacin resistance mutation per generation in C) *M. a. abscessus* strains, D) *M. a. massiliense* strains, or D) in all strains tested that are part of a dominant cluster or not. Mean +/- SD is displayed. In C-D, n=3 biological replicates. In E, each point represents the average mutation probability for a single strain. p-value derived from two-tailed, unpaired t-test.

Methods

Data Sources and Description: WGS data were curated from published studies[4,7,10,12,21–23] and additional data were downloaded from the NCBI Sequence Read Archive (SRA). A search of "abscessus" was conducted on October 4, 2019 using the filters "DNA" and "Illumina". Sequences were selected that had an associated date of collection with the year at minimum. Collection dates were obtained either from the literature, SRA metadata table, or provided by the authors. A summary of all samples used in this study is provided in Extended Data Table 1. Raw sequencing reads were downloaded using the NCBI SRA toolkit[24].

Quality control of Illumina reads: Reads were trimmed and filtered with trimmomatic[25]. To detect contaminated samples, the mean GC content of the reads were compared to a modelled normal distribution of GC content using fastqc[26]. If the sum of the deviations from the normal distribution represented more than 30% of the reads, the sequencing run was excluded from further analysis.

Subspecies assignment and genome assembly: Multiple sequencing runs corresponding to one biological sample were combined into one file. Reads were then assembled *de novo* using SPAdes[27]. Assemblies were compared to a reference sequence for each of the three subspecies (Supplementary Data Table 1) and a whole-genome based average nucleotide identity (gANI) score was calculated using fastANI[28]. The resulting alignments were assigned to a subspecies

based on having gANI of at least 98% with exactly one reference strain. Isolates that did not have at least 98% ANI with any reference strain were excluded. No isolates matched more than one reference genome. After assigning isolates to a subspecies, reads were mapped to the corresponding reference genome using BWA MEM[29]. After alignment, isolates with <80% coverage of the reference genome at a depth of at least 20x or with missing data at >30% of sites were excluded.

Variant calling and SNP filtering: Variants were called using Pilon[30]. We excluded ambiguous calls as wells as indels and MNVs. We also excluded calls with low coverage using a minimum depth of either 10% of the mean coverage, or 5, whichever was greater (default settings for Pilon –mindepth). We used bcftools[31] to exclude calls with mapping quality or base quality scores < 20.

Core genome inference: Unlike the professional mycobacterial pathogens *M. tuberculosis* or *M. leprae*, which have small accessory genomes, *M. abscessus* has a large, open accessory genome[32]. To define the core genome for phylogenetic analysis and to exclude loci that are highly divergent from the reference sequence, we masked all loci for downstream analysis where read depth was <20x in more than 5% of the isolates in our sample set. The remaining loci were compared to an estimate of the core genome calculated by Roary[33], and the two methods yielded nearly identical results. We further excluded regions with average mapping quality scores or average based quality scores <20. Finally, we used GenMap [34] to calculate mappability scores across each reference genome as defined in reference[35]. We then calculated a mappability pileup score for each base position as described in reference[36] and excluded loci where the mappability pileup score was <95% from downstream analysis. In total, we excluded 14.4%, 13.5%, and 15.1% of the *M. a. abscessus*, *M. a. massiliense*, and *M. a. bolletii* reference genome length, respectively.

561 Phylogenetic tree inference: A full-length sequence alignment was created using a custom script,
562 masking loci excluded by our filtering criteria described above. Gubbins[37] was used to predict and
563 mask regions of variation produced by recombination from the full-length alignment. A
564 recombination-free SNP alignment generated by Gubbins was then used to build a phylogeny for
565 each subspecies using IQ-TREE[38], using the ModelFinder Plus (-mfp) option and 1000 bootstrap
566 replicates. Clusters were defined as previously described[4] using a one-dimensional scanning
567 statistic to identify clades with a distribution of branch lengths that is shorter than the distribution
568 of branch lengths in the rest of the tree[39].
569
570 Coalescent analysis: Temporal signal was assessed using root-to-tip regression. In both *M. a.*
571 *abscessus* and *M. a. massiliense* subspecies trees and all three major clusters, a slightly negative
572 slope was observed, indicated lack of temporal signal. We recognized that the high degree of
573 clustering and short time span over which the clustered isolates were sampled may confound the
574 genetic temporal signal. To address this, we pruned the trees down to taxa that preserved 95%
575 of the relative tree length (RTL) of the original trees using Treemmer[40]. A threshold of 95%
576 eliminated most of the dense clustering, but preserved the long branches of the original tree
577 (Figure 2B, Figure S2B). Using the pruned tree, we observed evidence of temporal signal in the
578 MAB subspecies using root-to-tip regression. We generated a SNP alignment including only the
579 taxa present in the pruned *M. a. abscessus* tree and used this as input for coalescent analysis
580 using BEAST2[14]. ModelTest-NG[41] was used to select the site model GTR+4. MegaX[42] was used
581 to perform a maximum likelihood test to determine that a relaxed clock model is best suited for
582 our data. This choice was confirmed using the nested sampling algorithm to compare marginal
583 likelihoods for a strict v. relaxed clock model. We then used nested sampling to compare various
584 tree priors. We using Bayesian Evaluation of Temporal Signal (BETS) to confirm the presence of
585 temporal signal by comparing marginal likelihoods when the tip dates were used to those when
586 all samples were assumed to be isochronous (Extended Data Table 3). Based on marginal

likelihood values, we ran both a coalescent constant population model and a Bayesian skyline coalescent model, assuming a relaxed clock and including the sampling dates for both models. We used the ML phylogeny of the pruned dataset as a starting tree. For each model we ran two independent chains for at least 100 million states to ensure convergence.

Phylogenetic dating: To attempt to date the full MAB phylogeny, we ran both coalescent constant population and Bayesian skyline coalescent models assuming a relaxed clock without sampling dates. We set the mean UCLD clock rate to the values estimated from our coalescent analysis of the pruned tree. We ran each chain for at least 100 million states.

Estimation of mutation rate within-host: We identified 90 patients with two or more *M. a. abscessus* isolates. Because coinfection with multiple *M. abscessus* clones is common in cystic fibrosis patients, we first sought to exclude any isolate pairs that represented distinct clonal infections. We selected a threshold of 20 SNPs by comparing the distribution of all possible within-host isolate pairs to the distribution of pairwise SNP distances within *Mab* clusters. We further excluded any isolates where >20% of the genome is predicted to be rearranged by recombination. For the remaining isolate pairs we regressed the pairwise SNP distance between the first and last isolates sampled from each patient on the time between the collection of each sample. The slope of the regression line was used as an estimate of the number of SNPs accumulated over time.

Ancestry simulations: We used msprime[43] to simulate ancestries to model two subpopulations: (1) a “clustered” subpopulation (A) and (2) an “unclustered” subpopulation (B). We assumed a constant population size and initially set the total effective population size (N_e) to 8000, the N_e estimated in our coalescent analysis of the pruned *Mab* tree. We chose a range of realistic N_e for subpopulation A, N_e^A by running a separate coalescent analysis of *M. a. abscessus* cluster 1 using BEAST, assuming a constant population size, relaxed clock, and a range of UCLD clock rates

spanning $1.7x10^{-7}$ SNPs/site/year, as previously reported for this cluster by Ruis et al. (2021) to $8.5x10^{-6}$ SNPs/site/year, a value well above the 95% HPD interval for our estimate of the clock rate in the pruned tree (Extended Data Table 4). We assumed the N_e of subpopulation B to be: $N_e^B = N_e^{total}-N_e^A$. The number of samples and sampling dates supplied to the model for subpopulations A and B are drawn from the true values for *Mab* cluster 1 and from all "unclustered" isolates in the tree, respectively. We assumed an initial mutation rate of $1x10^{-9}$ mutations/generation with a sequence length of 5Mb and a divergence time of 30,000 generations between subpopulations A and B. We also assumed the nucleotide subsitution model estimated using BEAST.

We first simulated a scenario where the mutation rate remains constant, varying N_e^A over the range shown in Extended Data Table 4. For each simulated ancestry we overlaid mutation events, supplying the model with a starting substitution rate of $1x10^{-9}$ mutations/generation, a nucleotide substitution model estimated using BEAST, and a sequence length of 5Mb. We then extracted the simulated genotypes and constructed a neighbor joining (NJ) tree. The NJ tree was used to exclude any simulations where the two subpopulations did not exhibit reciprocal monophyly. We used the extracted genotypes to estimate the degree of clustering in each tree by comparing the mean pairwise SNP distance in subpopulation A (d_A) to the mean pairwise SNP distance in subpopulation B (d_B). For each simulated condition we performed 1000 replicates. To simulate ancestries with a mutation rate change, we repeated the above procedure conservatively assuming $N_e^A = 718$ (Extended Data Table 4). We modeled a per-generation mutation rate change starting at the common ancestor node for subpopulation A and ranging from 1-fold (no change) to 1/25-fold spanning a range of reasonable rate changes based on the range of clock rate estimates observed in this study and reported in the literature (Figure 2B). For all simulated conditions, we the simulation over a range of values for N_e^{total} spanning the 95% HPD intervals for the N_e estimates using the Treemmer tree under both the constant coalescent and coalescent skyline tree priors.

Scan for variants enriched in host-adapted lineages: To search for variants associated with host-adapted MAB lineages, we first inferred the number of independent arisals in the MAB phylogeny for each SNP using SNPPar[44]. Briefly, SNPPar uses TreeTime to perform an ancestral sequence reconstruction at each node, then infers mutation events arising on each branch of the tree. We quantified the number of independent mutation events for each SNP. We considered only mutation events where the derived call was the minor allele and the ancestral call was the major allele. Because of the extreme phylogenetic clustering in *Mab*, we defined the major and minor alleles using the pruned alignment generated by Treemmer. For all homoplasic SNPs (occurring two or more times independently in the tree), we used Fisher's exact test to quantify the enrichment of that variant within phylogenetic clusters. We conducted two separate analyses: a) focusing on the three largest clusters in the *M. a. abscessus* tree (described in the main text), and b) considering all clusters identified by this approach. In each case we obtained similar results. For both analyses, full lists of variants ranked by their enrichment scores are provided in Supplementary Data. We also used SNPPar to identify all mutation events occurring on the branch ancestral to *M. a. massiliense* cluster 1.

M. abscessus culture: *M. abscessus* clinical isolates used for fluctuation assays were isolated from patients in Taiwan and in Boston, MA, USA. All *M. abscessus* strains were cultured in Middlebrook 7H9 broth (271310, BD Diagnostics, Franklin Lakes, NJ, USA) with 0.2% (v/v) glycerol, 0.05% (v/v) Tween-80 (P1754, Sigma-Aldrich, St. Louis, MO, USA), and 10% (v/v) OADC (90000-614, VWR, Radnor, PA, USA). Proliferation rates were determined by inoculating 5 mL media with 500,000 colony forming units (cfu), then measuring OD600 at 24 and 48 hours post-inoculation. Proliferation rate was calculated as follows: proliferation rate in doublings per day = $\log_2$(OD600 at 48 hours / OD600 at 24 hours).

Fluctuation Assay: Fluctuation assays were performed as described previously[17] with adaptations for *M. abscessus*. *M. abscessus* strains were grown to saturation, then diluted to an OD600 < 0.01 and grown overnight until cultures reached an OD600 = 0.6-0.8. These cultures were used for fluctuation assays as well as determination of baseline amikacin sensitivity. Baseline amikacin sensitivity was tested by spreading dilutions of 10 million, 100 million, or 1 billion cfu on agar 7H10 (262710, BD Diagnostics) + OADC (90000-614, VWR) + 300 µg/mL amikacin sulfate (A2324, Sigma-Aldrich) plates. For fluctuation assays, 5000 cfu were plated in 1 mL media in each of 21 wells of a 24-well culture plate (10861-558, VWR), and initial cultures were plated for cfu on 7H10 + OADC to confirm number of cells in initial culture. 24-well plates were incubated shaking at 150 rpm for 6 days at 37°C. 18 wells of each strain were plated onto 6-well plates containing 5 mL 7H10 agar + OADC + 300 µg/mL amikacin sulfate in each well. Amikacin was used as the antibiotic selection for the assay because all tested strains had low baseline resistance (Extended Data Table 5), which is required for the validity of the fluctuation assay. The remaining 3 wells from each strain were diluted and plated on 7H10 + OADC plates to enumerate average final cfu. Colonies on all agar plates were counted after 5 days incubation at 37°C. Mutation rate per generation per total number of bases that can be mutated to confer amikacin resistance was calculated using the Shinyflan application for the flan R package[17] using the Maximum Likelihood estimation method, assumption of unknown fitness effects of mutations, the Exponential (LD model) distribution of mutant lifetime, and a Winsor parameter of 1024. One strain (BWH-E) was excluded from analysis due to highly variable results across replicates (Figure S6B).

Code Availability

All custom scripts are available at:
https://github.com/nicolettacommins/mab_mutation_rates_2022.

690 **Extended Data**

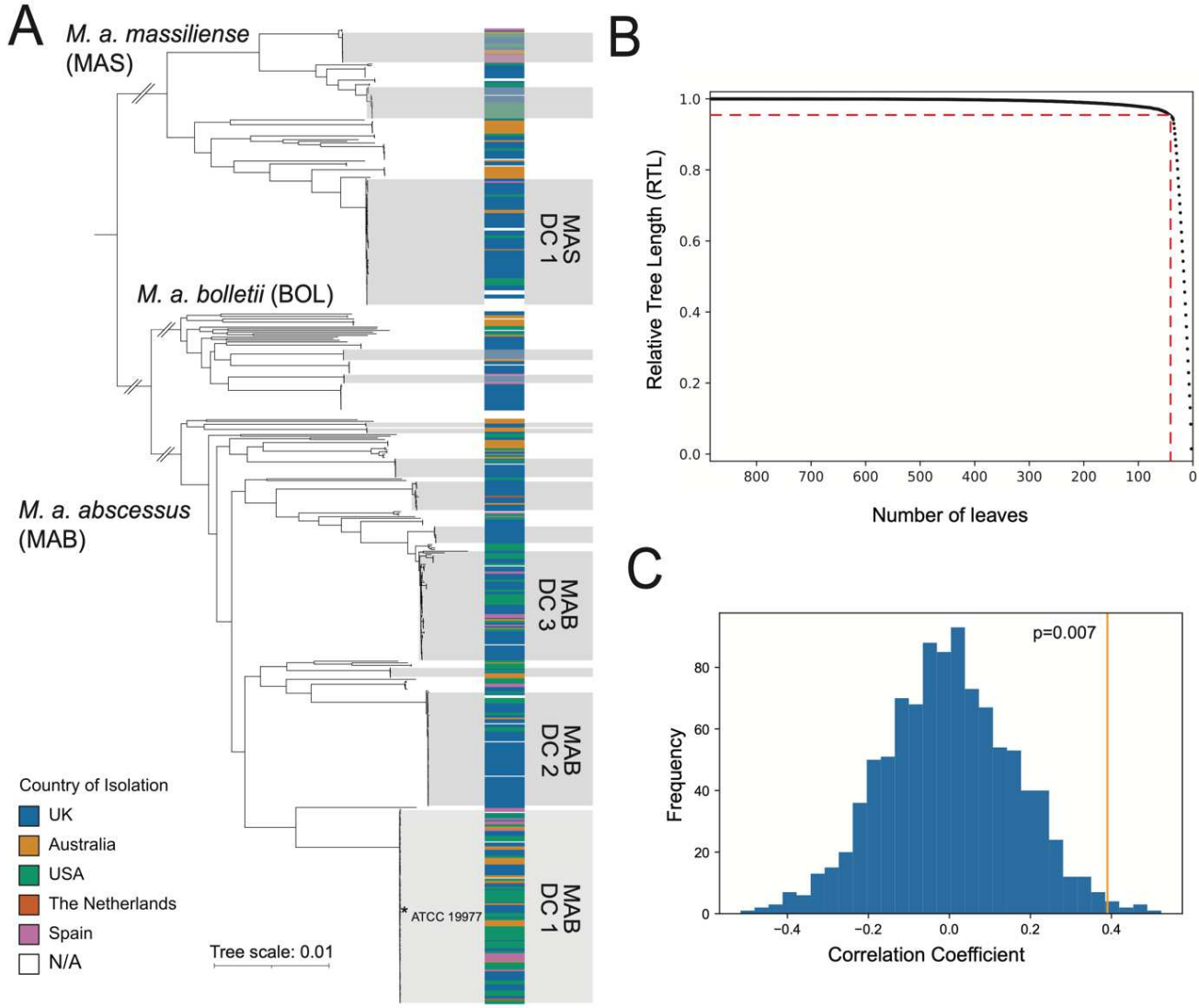

691

692 **Extended Data Figure 1. *M. a. abscessus* clusters and inference of temporal signal (related to Figure 1).** A) Full species tree showing all clusters identified including DCs and non DC clusters.
693 DCs are labeled. B) The relative tree length (RTL) v. the number of leaves remaining in the tree after each cycle of pruning with Treemmer. RTL is a measure of the diversity in the pruned tree relative to the original tree. The dotted red line indicates where the RTL is 95%, corresponding to 38 isolates. C) Permutation test for significance of temporal signal in the pruned *M. a. abscessus* tree. We randomly shuffled the dates of collection and root-to-tip distances from the pruned subspecies tree 1000 times. For each permutation we calculated Pearson's correlation between the collection dates and root-to-tip distances to estimate an empirical p-value = 0.007.

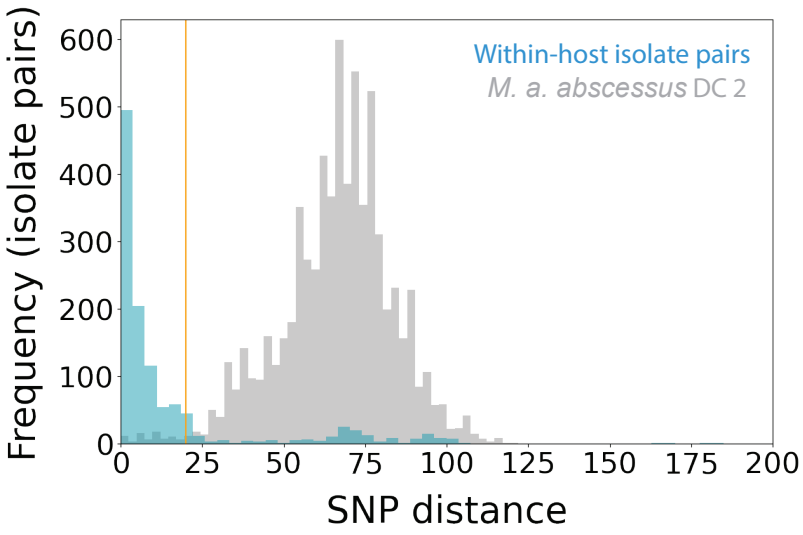

Extended Data Figure 2. SNP distance threshold for within-host isolate pairs (related to Figure 2A). Distribution of SNP distances between all possible within-host isolate pairs in *M. a. abscessus* compared to SNP distances between all possible isolate pairs within *M. a. abscessus* DC 2.

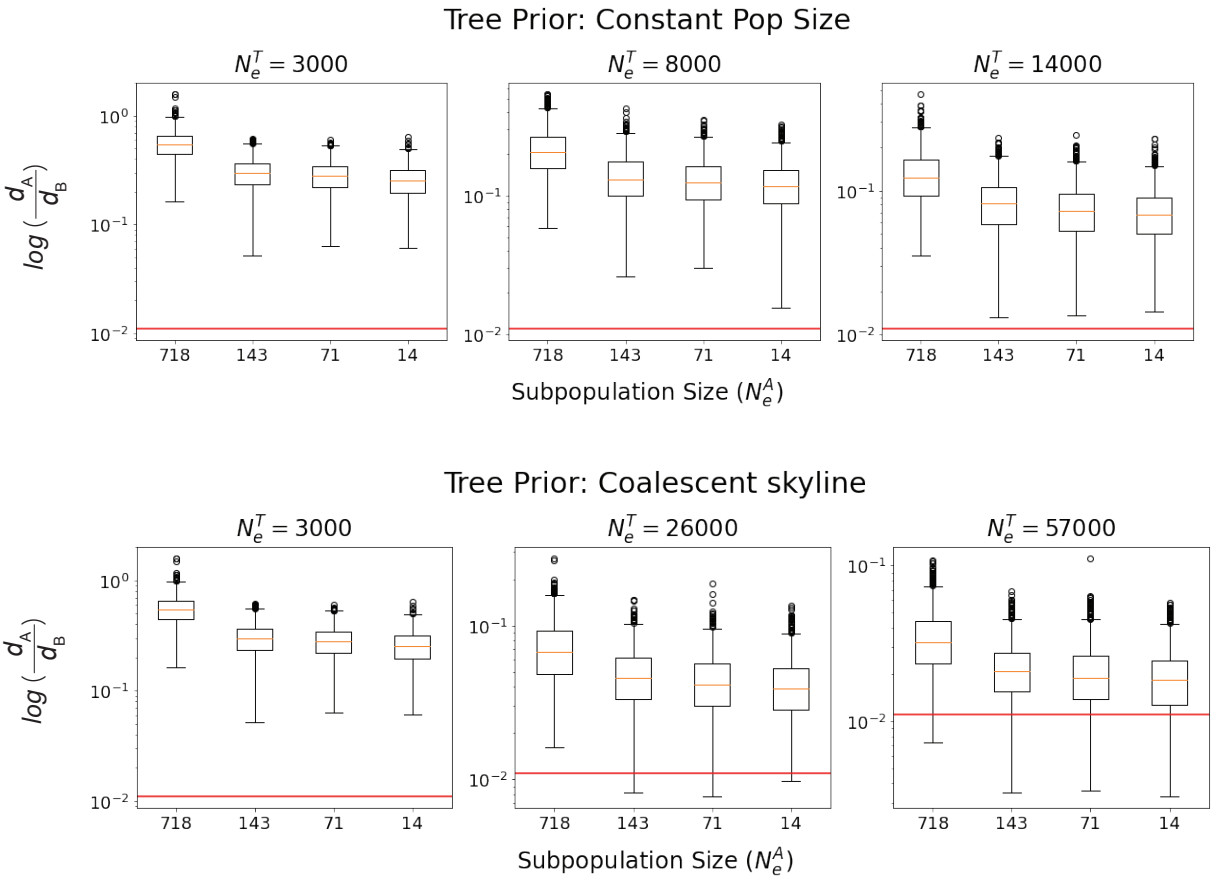

Extended Data Figure 3. Ancestry simulations across a range of possible population sizes (related to Figure 3A). Boxplots showing the degree of phylogenetic clustering in subpopulation A relative to subpopulation B (Figure 3A) over a range of effective population sizes of subpopulation A (N_e^A) and a range of total effective population sizes (N_e^T) spanning the 95% confidence intervals estimated using BEAST under a constant population size model (top) and a Bayesian coalescent skyline model (bottom). The top center panel recapitulates figure 3B.

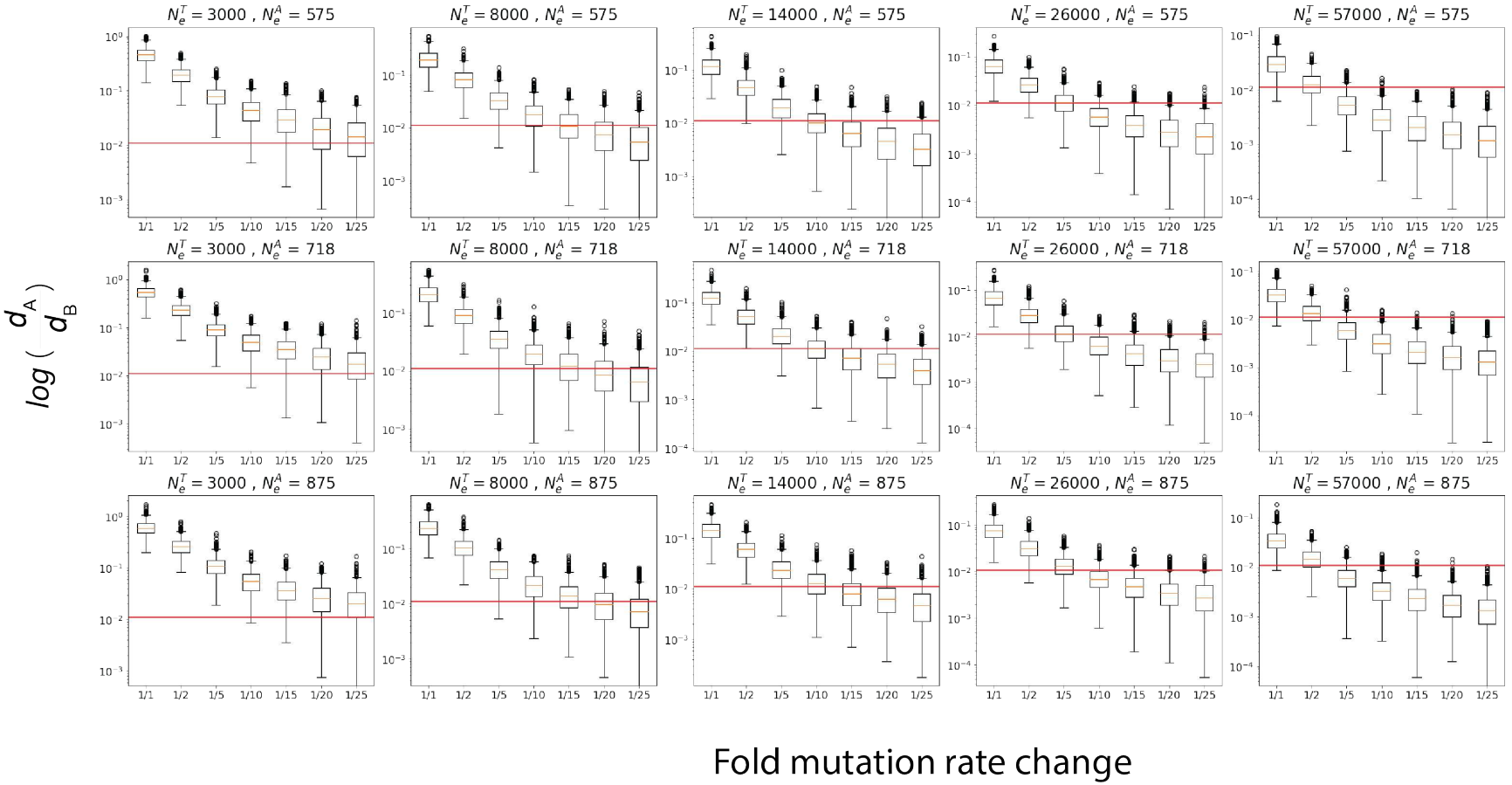

Extended Data Figure 4. Ancestry simulations over a range of population sizes and mutation rate changes (Related to Figure 3B,C). Boxplot showing the degree of phylogenetic clustering in subpopulation A relative to subpopulation B over a range of mutation rate changes. Each set of simulations is repeated over a range of effective population sizes of subpopulation A (N_e^A) and a range of total effective population sizes (N_e^T) spanning the 95% confidence intervals estimated using BEAST assuming a constant population size tree prior. The panel in which N_e^T=8000 and N_e^A=718 recapitulates Figure 3B.

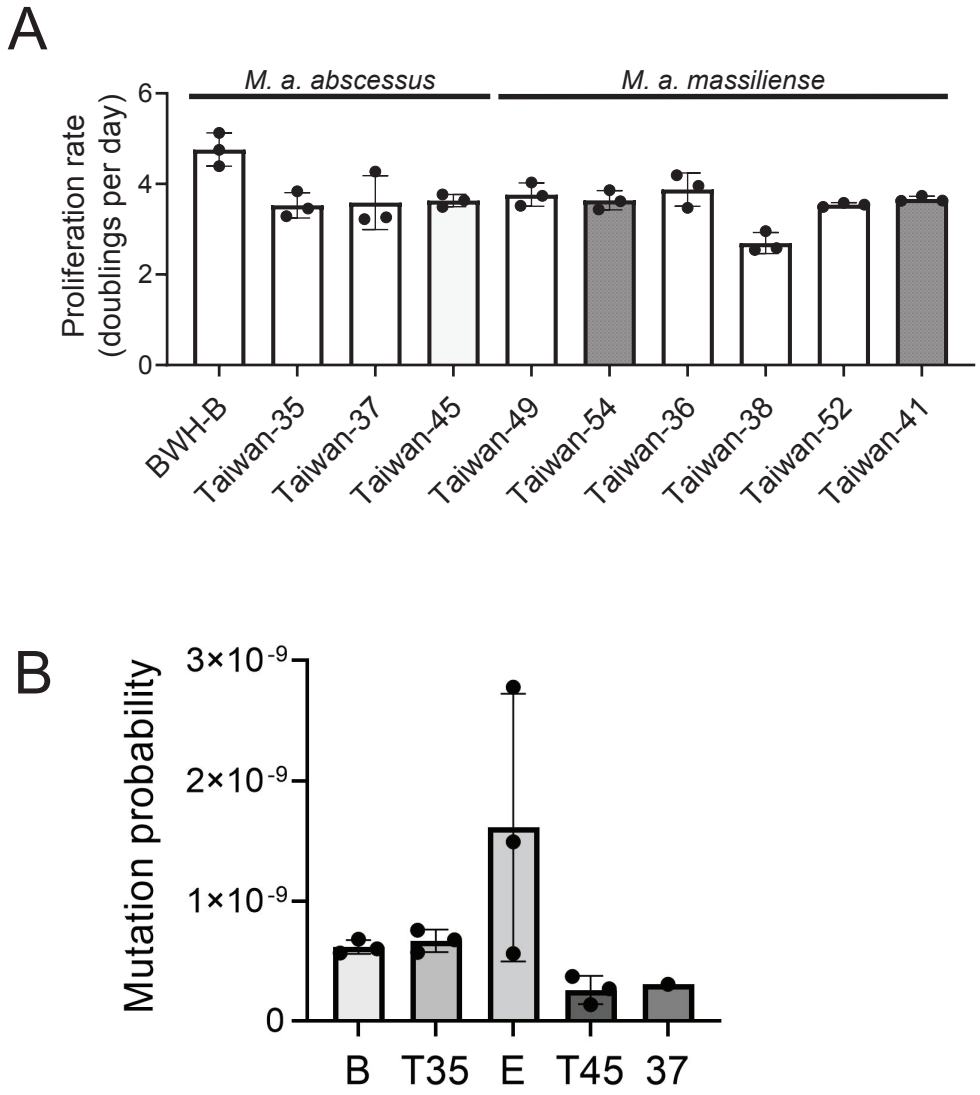

Extended Data Figure 5. Growth rates and mutation probability of *M. abscessus* strains. (Related to Figure 4C-E). A) Growth rates of all isolates used in fluctuation assays. B) Probability of acquiring an amikacin resistance mutation per generation in *M. a. abscessus* strains including BWH-E. Data for BWH-B, Taiwan-35, Taiwan-37, and Taiwan-45 are reproduced from Figure 4C. Mean +/- SD for 3 biological replicates is displayed.

749 **Extended Data Table 1**. Isolates used in this study

Number of samples	BioProject ID	Citation
854	PRJEB2779	Bryant, J et al. 2016. “Emergence and Spread of a Human-Transmissible Multidrug-Resistant Nontuberculous Mycobacterium.” *Science* 354 (6313): 751–57.
190	PRJNA319839	Hasan, NA et al. 2019. “Population Genomics of Nontuberculous Mycobacteria Recovered from United States Cystic Fibrosis Patients.” *bioRxiv*. https://doi.org/10.1101/663559.
173	PRJEB7058	Everall, I et al. 2017. “Genomic Epidemiology of a National Outbreak of Post-Surgical Mycobacterium Abscessus Wound Infections in Brazil.” *Microbial Genomics* 3 (5): e000111.
141	PRJEB31559	Doyle, RM et al. 2019. “Cross-Transmission Is Not the Source of New Mycobacterium Abscessus Infections in a Multi-Centre Cohort of Cystic Fibrosis Patients.” *Clinical Infectious Diseases: An Official Publication of the Infectious Diseases Society of America*, June. https://doi.org/10.1093/cid/ciz526.
69	PRJNA420644	Lipworth, S. *et al.* Whole-Genome Sequencing for Predicting Clarithromycin Resistance in Mycobacterium abscessus. *Antimicrob. Agents Chemother.* **63**, (2019)
17	PRJNA439313	Yan, J. *et al.* Investigating transmission of Mycobacterium abscessus amongst children in an Australian cystic fibrosis centre. *J. Cyst. Fibros.* **19**, 219–224 (2020)
11	PRJNA297030	Unpublished
1	PRJNA447908	Unpublished
1	PRJNA495001	Chhotaray, C. *et al.* Comparative Analysis of Whole-Genome and Methylome Profiles of a Smooth and a Rough Mycobacterium abscessus Clinical Strain. *G3* **10**, 13–22 (2020)
1	PRJEB1520	Unpublished
1	PRJNA347845	Fogelson, S. B. *et al.* Variation among human, veterinary and environmental Mycobacterium chelonae-abscessus complex isolates observed using core genome phylogenomic analysis, targeted gene comparison, and anti-microbial susceptibility patterns. *PLoS One* **14**, e0214274 (2019)
1	PRJNA566387	Pearce, C. *et al.* Inhaled tigecycline is effective against Mycobacterium abscessus in vitro and in vivo. *J. Antimicrob. Chemother.* **75**, 1889–1894 (2020)
1	PRJNA401495	Unpublished

750

751

752

Extended Data Table 2. Description of Isolation Sources

Isolation Source	Number of samples (%)
Pulmonary	1181 (80.8%)
Skin and soft tissue swab or biopsy	185 (12.7%)
Lymph node	8 (0.5%)
Environmental	4 (0.2%)
CSF	3 (0.2%)
Blood	2 (0.1%)
Feces	2 (0.1%)
Clinical isolates from unknown source	76 (5.2%)

Extended Data Table 3. Results from Bayesian Evaluation of Temporal Signal

Model	Marginal likelihood (SD)
Relaxed clock, constant population size (with dates)	-7144301.64 (21.42)
Relaxed clock, constant population size (without dates)	-7144579.04 (21.01)

Comparison of the marginal likelihoods with sampling dates and without sampling dates yields the following Bayes Factor (BF) calculation: $Log_{10}(BF) = 277.4$

Extended Data Table 4. BEAST estimated Ne for the 'clustered' subpopulation A under a range of assumed clock rates

Clock rate (SNPs/site/year)	N_e^A [95% HPD]
$1.7x10^{-7}$ [a]	718.99 [575.06, 875.16]
$8.5x10^{-7}$	142.79 [116.38, 175.52]
$1.7x10^{-6}$	71.75 [57.57, 87.07]
$8.5x10^{-6}$	14.27 [11.47, 17.35]

[a] Mutation rate estimated for *M. a. abscessus* cluster 1 by Ruis et al.[13]

Extended Data Table 5. Baseline Rates of Resistance to Amikacin in Clinical Isolates

Strain	Fraction of cells resistant to amikacin
Mas-Taiwan-36	n.d.
Mas-Taiwan-38	$8.77x10^{-8}$
Mas-Taiwan-41	n.d.
Mas-Taiwan-52	$1.59x10^{-8}$
Mas-Taiwan-49	n.d.
Mas-Taiwan-54	$5x10^{-8}$
Mab-BWH-B	$1x10^{-8}$
Mab-BWH-E	$1x10^{-8}$
Mab-Taiwan-35	$1x10^{-8}$
Mab-Taiwan-37	n.d.
Mab-Taiwan-45	n.d.

n.d. = no resistant colonies were detected

References

1. Adjemian, J., Olivier, K. N. & Prevots, D. R. Epidemiology of Pulmonary Nontuberculous Mycobacterial Sputum Positivity in Patients with Cystic Fibrosis in the United States, 2010-2014. *Ann. Am. Thorac. Soc.* **15**, 817–826 (2018).
2. Lee, M.-R. *et al.* Mycobacterium abscessus Complex Infections in Humans. *Emerg. Infect. Dis.* **21**, 1638–1646 (2015).
3. Nessar, R., Cambau, E., Reyrat, J. M., Murray, A. & Gicquel, B. Mycobacterium abscessus: a new antibiotic nightmare. *J. Antimicrob. Chemother.* **67**, 810–818 (2012).
4. Bryant, J. M. *et al.* Emergence and spread of a human-transmissible multidrug-resistant nontuberculous mycobacterium. *Science* **354**, 751–757 (2016).
5. Bange, F. C., Brown, B. A., Smaczny, C., Wallace, R. J., Jr & Böttger, E. C. Lack of transmission of mycobacterium abscessus among patients with cystic fibrosis attending a single clinic. *Clin. Infect. Dis.* **32**, 1648–1650 (2001).
6. Olivier, K. N. *et al.* Nontuberculous mycobacteria. I: multicenter prevalence study in cystic fibrosis. *Am. J. Respir. Crit. Care Med.* **167**, 828–834 (2003).
7. Doyle, R. M. *et al.* Cross-transmission is not the source of new Mycobacterium abscessus infections in a multi-centre cohort of cystic fibrosis patients. *Clin. Infect. Dis.* (2019) doi:10.1093/cid/ciz526.
8. Sermet-Gaudelus, I. *et al.* Mycobacterium abscessus and children with cystic fibrosis. *Emerg. Infect. Dis.* **9**, 1587–1591 (2003).
9. Lipworth, S. *et al.* Epidemiology of Mycobacterium abscessus in England: an observational study. *The Lancet Microbe* (2021) doi:10.1016/S2666-5247(21)00128-2.
10. Harris, K. A. *et al.* Whole-genome sequencing and epidemiological analysis do not provide evidence for cross-transmission of mycobacterium abscessus in a cohort of pediatric cystic fibrosis patients. *Clin. Infect. Dis.* **60**, 1007–1016 (2015).

11. Tortoli, E. *et al.* Mycobacterium abscessus in patients with cystic fibrosis: low impact of inter-human transmission in Italy. *Eur. Respir. J.* **50**, (2017).
12. Everall, I. *et al.* Genomic epidemiology of a national outbreak of post-surgical Mycobacterium abscessus wound infections in Brazil. *Microb Genom* **3**, e000111 (2017).
13. Ruis, C. *et al.* Dissemination of Mycobacterium abscessus via global transmission networks. *Nature Microbiology* 1–10 (2021) doi:10.1038/s41564-021-00963-3.
14. Bouckaert, R. *et al.* BEAST 2.5: An advanced software platform for Bayesian evolutionary analysis. *PLoS Comput. Biol.* **15**, e1006650 (2019).
15. Houghton, J. *et al.* Important role for Mycobacterium tuberculosis UvrD1 in pathogenesis and persistence apart from its function in nucleotide excision repair. *J. Bacteriol.* **194**, 2916–2923 (2012).
16. Sinha, K. M., Unciuleac, M.-C., Glickman, M. S. & Shuman, S. AdnAB: a new DSB-resecting motor-nuclease from mycobacteria. *Genes Dev.* **23**, 1423–1437 (2009).
17. Krašovec, R. *et al.* Measuring Microbial Mutation Rates with the Fluctuation Assay. *J. Vis. Exp.* (2019) doi:10.3791/60406.
18. Ho, S. Y. W., Shapiro, B., Phillips, M. J., Cooper, A. & Drummond, A. J. Evidence for time dependency of molecular rate estimates. *Syst. Biol.* **56**, 515–522 (2007).
19. Huffnagle, G. B., Dickson, R. P. & Lukacs, N. W. The respiratory tract microbiome and lung inflammation: a two-way street. *Mucosal Immunol.* **10**, 299–306 (2017).
20. Curti, E., Smerdon, S. J. & Davis, E. O. Characterization of the helicase activity and substrate specificity of Mycobacterium tuberculosis UvrD. *J. Bacteriol.* **189**, 1542–1555 (2007).
21. Bryant, J. M. *et al.* Whole-genome sequencing to identify transmission of Mycobacterium abscessus between patients with cystic fibrosis: a retrospective cohort study. *Lancet* **381**, 1551–1560 (2013).
22. Hasan, N. A. *et al.* Population Genomics of Nontuberculous Mycobacteria Recovered from United States Cystic Fibrosis Patients. *bioRxiv* 663559 (2019) doi:10.1101/663559.

23. Shaw, L. P. *et al.* Children with cystic fibrosis are infected with multiple subpopulations of Mycobacterium abscessus with different antimicrobial resistance profiles. *Clin. Infect. Dis.* (2019) doi:10.1093/cid/ciz069.
24. Download : Software : Sequence Read Archive : NCBI/NLM/NIH. https://trace.ncbi.nlm.nih.gov/Traces/sra/sra.cgi?view=software.
25. Bolger, A. M., Lohse, M. & Usadel, B. Trimmomatic: a flexible trimmer for Illumina sequence data. *Bioinformatics* **30**, 2114–2120 (2014).
26. Babraham Bioinformatics - FastQC A Quality Control tool for High Throughput Sequence Data. https://www.bioinformatics.babraham.ac.uk/projects/fastqc/.
27. Prjibelski, A., Antipov, D., Meleshko, D., Lapidus, A. & Korobeynikov, A. Using SPAdes De Novo Assembler. *Curr. Protoc. Bioinformatics* **70**, e102 (2020).
28. Jain, C., Rodriguez-R, L. M., Phillippy, A. M., Konstantinidis, K. T. & Aluru, S. High throughput ANI analysis of 90K prokaryotic genomes reveals clear species boundaries. *Nat. Commun.* **9**, 5114 (2018).
29. Li, H. Aligning sequence reads, clone sequences and assembly contigs with BWA-MEM. *arXiv [q-bio.GN]* (2013).
30. Walker, B. J. *et al.* Pilon: an integrated tool for comprehensive microbial variant detection and genome assembly improvement. *PLoS One* **9**, e112963 (2014).
31. Li, H. A statistical framework for SNP calling, mutation discovery, association mapping and population genetical parameter estimation from sequencing data. *Bioinformatics* **27**, 2987–2993 (2011).
32. Choo, S. W. *et al.* Genomic reconnaissance of clinical isolates of emerging human pathogen Mycobacterium abscessus reveals high evolutionary potential. *Sci. Rep.* **4**, 4061 (2014).
33. Page, A. J. *et al.* Roary: rapid large-scale prokaryote pan genome analysis. *Bioinformatics* **31**, 3691–3693 (2015).

34. Pockrandt, C., Alzamel, M., Iliopoulos, C. S. & Reinert, K. GenMap: ultra-fast computation of genome mappability. *Bioinformatics* **36**, 3687–3692 (2020).
35. Derrien, T. *et al.* Fast computation and applications of genome mappability. *PLoS One* **7**, e30377 (2012).
36. Marin, M. *et al.* Benchmarking the empirical accuracy of short-read sequencing across the M. tuberculosis genome. *Bioinformatics* (2022) doi:10.1093/bioinformatics/btac023.
37. Croucher, N. J. *et al.* Rapid phylogenetic analysis of large samples of recombinant bacterial whole genome sequences using Gubbins. *Nucleic Acids Res.* **43**, e15 (2015).
38. Minh, B. Q. *et al.* IQ-TREE 2: New Models and Efficient Methods for Phylogenetic Inference in the Genomic Era. *Mol. Biol. Evol.* **37**, 1530–1534 (2020).
39. Harris, S. TreeGubbins. (2016).
40. Menardo, F. *et al.* Treemmer: a tool to reduce large phylogenetic datasets with minimal loss of diversity. *BMC Bioinformatics* **19**, 164 (2018).
41. Darriba, D. *et al.* ModelTest-NG: A New and Scalable Tool for the Selection of DNA and Protein Evolutionary Models. *Mol. Biol. Evol.* **37**, 291–294 (2020).
42. Kumar, S., Stecher, G., Li, M., Knyaz, C. & Tamura, K. MEGA X: Molecular Evolutionary Genetics Analysis across Computing Platforms. *Mol. Biol. Evol.* **35**, 1547–1549 (2018).
43. Kelleher, J. & Lohse, K. Coalescent Simulation with msprime. in *Statistical Population Genomics* (ed. Dutheil, J. Y.) 191–230 (Springer US, 2020). doi:10.1007/978-1-0716-0199-0_9.
44. Edwards, D. J., Duchêne, S., Pope, B. & Holt, K. E. SNPPar: identifying convergent evolution and other homoplasies from microbial whole-genome alignments. *bioRxiv* 2020.07.08.194480 (2020) doi:10.1101/2020.07.08.194480.

895

896

897

898

899

900

901

902

903

904

905

906

907

908

909

Supplementary Files

This is a list of supplementary files associated with this preprint. Click to download.

- mabmutRatenatureMicrosupplement.pdf